Computer Methods in Applied Mechanics and Engineering 199 (2010) 2765–2778

Contents lists available at ScienceDirect

Computer Methods in Applied Mechanics and Engineering

journal homepage: www.elsevier.com/locate/cma

A phase field model for rate-independent crack propagation: Robust algorithmic implementation based on operator splits

Christian Miehe *, Martina Hofacker, Fabian Welschinger

Institute of Applied Mechanics (CE) Chair I, University of Stuttgart, Pfaffenwaldring 7, 70550 Stuttgart, Germany

ARTICLE INFO

Article history:
Received 4 January 2010
Received in revised form 14 April 2010
Accepted 15 April 2010
Available online 7 May 2010

Keywords:
Fracture
Crack propagation
Phase fields
Gradient-type damage
Incremental variational principles
Finite elements
Coupled multi-field problem

ABSTRACT

The computational modeling of failure mechanisms in solids due to fracture based on *sharp* crack discontinuities suffers in situations with complex crack topologies. This can be overcome by a *diffusive* crack modeling based on the introduction of a crack phase field. Following our recent work [C. Miehe, F. Welschinger, M. Hofacker, Thermodynamically-consistent phase field models of fracture: Variational principles and multi-field fe implementations, International Journal for Numerical Methods in Engineering DOI:10.1002/nme.2861] on phase-field-type fracture, we propose in this paper a new variational framework for rate-independent diffusive fracture that bases on the introduction of a *local history field*. It contains a maximum reference energy obtained in the deformation history, which may be considered as a measure for the maximum tensile strain obtained in history. It is shown that this local variable drives the evolution of the crack phase field. The introduction of the history field provides a very transparent representation of the balance equation that governs the diffusive crack topology. In particular, it allows for the construction of a new algorithmic treatment of diffusive fracture. Here, we propose an extremely *robust operator split scheme* that successively updates in a typical time step the history field, the crack phase field and finally the displacement field. A regularization based on a viscous crack resistance that even enhances the robustness of the algorithm may easily be added. The proposed algorithm is considered to be the canonically simple scheme for the treatment of diffusive fracture in elastic solids. We demonstrate the performance of the phase field formulation of fracture by means of representative numerical examples.

1. Introduction

The prediction of failure mechanisms due to crack initiation and propagation in solids is of great importance for engineering applications. Following the classical treatments of Griffith [2] and Irwin [3], cracks propagate if the energy release rate reaches a critical value. The Griffith theory provides a criterion for crack propagation but is insufficient to determine curvilinear crack paths, crack kinking and branching angles. In particular, such a theory is unable to predict crack initiation. These defects of the classical Griffith-type theory of brittle fracture can be overcome by variational methods based on energy minimization as suggested by Francfort & Marigo [4], see also Bourdin, Francfort & Marigo [5], Dal Maso & Toader [6] and Buliga [7]. The regularized setting of their framework, considered in Bourdin, Francfort & Marigo [8,5], is obtained by Γ-convergence inspired by the work on image segmentation by Mumford & Shah [9]. We refer to Ambrosio & Tortorelli [10] and the reviews of Dal Maso [11] and Braides [12,13] for details on Γ-convergent approximations of free discontinuity problems. The approximation regularizes a sharp crack surface topology in the solid by diffusive crack zones governed by a scalar auxiliary variable. This variable can be considered as a phase field which interpolates between the unbroken and the broken state of the material. Conceptually similar are recently outlined phase field approaches to brittle fracture based on the classical Ginzburg-Landau type evolution equation as reviewed in Hakim & Karma [14], see also Karma, Kessler & Levine [15] and Eastgate et al. [16]. In contrast to the above mentioned rate-independent approach, these models are *fully* viscous in nature and mostly applied to dynamic fracture. The phase field approaches to fracture offer important new perspectives towards the theoretical and computational modeling of complex crack topologies. Recall that finite-element-based numerical implementations of sharp crack discontinuities, such as interface element formulations, element and nodal enrichment strategies suffer in the case of three-dimensional applications with crack branching. Advanced XFEM-based methods for *sharp* crack propagation are outlined in Belytschko et al. [17,18] We also refer to the adaptive interface methods by Gürses & Miehe [19] and Miehe & Gürses [20,21] for the modeling of configurational-force-driven sharp crack propagation. In contrast, phase-field-type *diffusive* crack approaches avoid the modeling of discontinuities and can be implemented in a straightforward manner by coupled multi-field finite element solvers. In the recent work Miehe, Welschinger & Hofacker [1], we outlined a general

* Corresponding author. Tel.: +49 711 685 66379.
E-mail address: christian.miehe@mechbau.uni-stuttgart.de (C. Miehe).
URL: http://www.mechbau.uni-stuttgart.de/ls1/ (C. Miehe).

0045-7825/$ – see front matter © 2010 Elsevier B.V. All rights reserved.
doi:10.1016/j.cma.2010.04.011

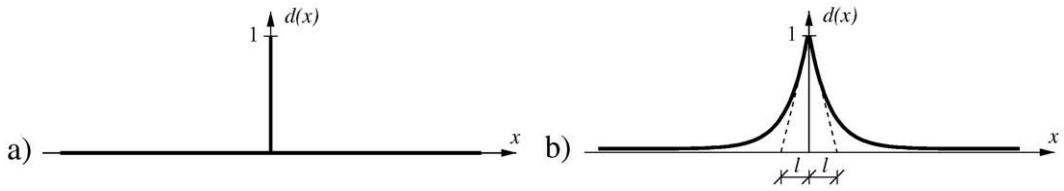

Fig. 1. Sharp and diffusive crack topology. a) Sharp crack at $x=0$. b) Diffusive crack at $x=0$ modeled with the length scale l in terms of the crack phase field d.

thermodynamically-consistent framework of phase field modeling in fracture mechanics and considered aspects of its numerical implementation. It overcomes some of the difficulties inherent in the above mentioned phase field approaches, by definition of fracture only in tension, precise characterization of the dissipation and introduction of the viscosity as a *regularization* of the rate-independent formulation. The numerical treatment was based on a *monolithic three-field saddle point principle*, that includes beside the displacement and fracture phase field a particular crack driving force field.

In this work, we develop a new model of phase-field-type fracture that substantially enhances our formulations in Miehe, Welschinger & Hofacker [1]. The key novel aspects are the formulation of the balance equation for the evolution of the phase field in terms of a strain-history source term, which allows an extremely simple and robust staggered solution of the two-field problem in terms of the algorithm summarized in Box 1. On the theoretical side, we outline an incremental variational formulation for a *rate-independent* evolution of the crack phase model. The important characteristic is the introduction of a *crack surface density function* that governs the dissipation in the diffusive fracture theory. The key observation then is that the possible discontinuous evolution of the phase field in time is driven by a *local history field*. It contains a maximum reference energy obtained in the deformation history, which may be considered as a measure for the maximum tensile strain obtained in history. It is shown that this local variable drives the evolution of the crack phase field. The introduction of the history field provides a very transparent representation of the balance equation that governs the evolution of the diffusive crack topology. It represents a source term in the balance equation for the phase-field. In order to stabilize post-critical solution paths, we may add a viscous regularization. This consists of the introduction of a viscous term that supplements the crack surface resistance. A particular ingredient is that the rate-independent limit is recovered by simply setting the viscosity to zero. This feature of the proposed theory is a very important element of a robust numerical implementation. The proposed approach is embedded in the theory of gradient-type materials with a characteristic length scale, such as outlined in the general context by Capriz [22], Mariano [23] and Fremond [24]. On the numerical side, we develop a *robust scheme* for the incremental update of the fracture phase field and the displacement field. It represents an operator split algorithm within a typical time step that allows a staggered update of the phase field and the displacement field. The central idea for the algorithmic decoupling of the coupled equations is an approximation of the current history field that provides the crack source term in the diffusive crack topology equation. The formulation results in *two linear problems* for the successive update of the phase field and the displacement field within a typical time step. The proposed staggered scheme is extremely robust. The formulation may be considered as a canonical framework for the implementation of phase-field-type fracture in the rate-independent setting.

We start our investigation in Section 2 with a descriptive motivation of a regularized crack topology based on a phase field. This treatment results in the definition of a *crack surface functional*, depending on the crack phase field, that Γ-converges for vanishing length-scale parameter to a sharp crack topology. We consider this crack functional as the crack surface itself and postulate that it should stay constant or grow for arbitrary loading processes. The next modeling step, discussed in Section 3, is concerned with the definition of *energy storage and dissipation functionals* which depend on the fracture phase field. Here, we consider stored energy functions where the degradation due to the growing phase field acts only on a properly defined positive (tensile) part of the stored energy. The dissipation functional is directly related to the evolution of the crack surface functional via a material parameter that represents the critical energy release. With the dissipation and energy functionals at hand, we derive the governing balance equations from an incremental variational principle. For the quasi-static processes under consideration, the coupled system of equations consists of the *static equilibrium condition* for the degraded stresses and the *balance equation for the phase field*. It characterizes a two-field problem with the displacement field and the phase-field as the primary variables. For this coupled field problem, we develop in Section 4 the new staggered solution scheme which contains minimizers for each partial problem. The discrete counterparts of the continuous variational principles results in two *linear* algebraic Euler equations for the algorithmically decoupled incremental problem. Finally, Section 5 outlines representative numerical examples which demonstrate the features and algorithmic robustness of the proposed phase field models of fracture.

2. Crack phase field and crack surface density function

2.1. Phase field approximation of crack topology

We motivate the construction of a variational principle of *diffusive crack topology* by a simple model problem. Following our work Miehe, Welschinger & Hofacker [1], we consider an infinitely expanded bar of cross-section Γ occupying the domain $\mathcal{B}=\Gamma\times L$ with $L=[-\infty,+\infty]$ and position $x\in L$ of its axis. Assume a crack of the bar at the axial position $x=0$, where Γ represents the fully-broken crack surface. This *sharp crack topology* may be described by an auxiliary field variable $d(x)\in[0,1]$, characterizing for $d=0$ the unbroken state and for $d=1$ the fully-broken state of the material. Fig. 1a gives a visualization. We denote the auxiliary variable $d(x)$ as the *crack phase field*. Clearly, such an approach is related to the continuum theory of damage, where the scalar damage field d describes in a homogenized macroscopic sense the development of micro-cracks and micro-voids. With this viewpoint in mind, we approximate the non-smooth phase field by the exponential function

$$d(x) = e^{-|x|/l}. \tag{1}$$

It smears out the crack over the axial domain L of the bar, representing a *regularized or diffusive crack topology* as depicted in Fig. 1b. The regularization is governed by the length scale parameter l and gives for $l\to 0$ the sharp crack topology. The exponential function (1) has the property $d(0)=1$ and $d(\pm\infty)=0$. Now observe that Eq. (1) is the solution of the homogeneous differential equation

$$d(x) - l^2 d''(x) = 0 \quad \text{in} \quad \mathcal{B} \tag{2}$$

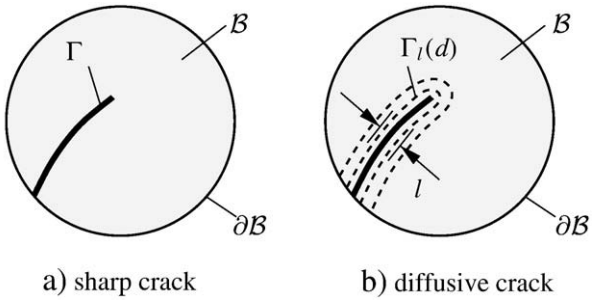

Fig. 2. Sharp and diffusive crack topology. a) Sharp crack surface Γ embedded into the solid $\mathcal{B}$. b) The regularized crack surface $\Gamma_l(d)$ is a functional of the crack phase field d.

subject to the above Dirichlet-type boundary conditions. This differential equation is the Euler equation of the variational principle

$$d = \text{Arg}\{\inf_{d\in W} I(d)\} \quad \text{with} \quad I(d) = \frac{1}{2}\int_{\mathcal{B}} \Big\{ d^2 + l^2 d'^2 \Big\} dV \tag{3}$$

and $W = \{d | d(0) = 1,\ d(\pm\infty) = 0\}$. The functional $I(d)$ can easily be constructed by integrating a Galerkin-type weak form of the differential Eq. (2). Now observe, that the evaluation of the functional for the solution (1) gives with $dV = \Gamma dx$ the identification $I(d = e^{-|x|/l}) = l\Gamma$, which relates the functional I to the crack surface Γ. As a consequence, we may introduce the functional

$$\Gamma_l(d) := \frac{1}{l} I(d) = \frac{1}{2l}\int_{\mathcal{B}} \Big\{ d^2 + l^2 d'^2 \Big\} dV \tag{4}$$

alternatively to Eq. $(3)_2$. Clearly, the minimization of this scaled functional also gives the regularized crack topology (1) depicted in Fig. 1b. However, the scaling by the length-scale parameter l has the consequence that the functional $\Gamma_l(d)$ may be *considered as the crack surface itself*. In the one-dimensional problem under consideration, the evaluation of $\Gamma_l(d)$ at the solution point gives for arbitrary length scales l the crack surface Γ. This property characterizes the functional Γ_l as an important ingredient of the subsequent constitutive modeling of diffusive crack propagation.

2.2. Introduction of a crack surface density function

The one-dimensional description of a *diffusive crack topology* can be extended to multi-dimensional solids in a straightforward manner. Let $\mathcal{B} \subset \mathcal{R}^\delta$, be the reference configuration of a material body with dimension $\delta \in [1\text{–}3]$ in space and $\partial\mathcal{B} \subset \mathcal{R}^{\delta-1}$ its surface as depicted in Fig. 2. In the subsequent treatment, we intend to study cracks in the solid evolving in the range $\mathcal{T} \subset \mathcal{R}$ of time. To this end, we introduce the time-dependent crack phase field

$$d : \begin{cases} \mathcal{B}\times\mathcal{T} \to [0,1] \\ (\boldsymbol{x}, t) \mapsto d(\boldsymbol{x}, t) \end{cases} \tag{5}$$

defined on the solid $\mathcal{B}$. Then, a multi-dimensional extension of the one-dimensional regularized crack functional Eq. (4), derived in Appendix A, reads

$$\Gamma_l(d) = \int_{\mathcal{B}} \gamma(d, \nabla d) dV, \tag{6}$$

where we have introduced the *crack surface density function* per unit volume of the solid

$$\boxed{\gamma(d, \nabla d) = \frac{1}{2l} d^2 + \frac{l}{2} |\nabla d|^2} \tag{7}$$

This function, which depends on the crack phase field d and its spatial gradient ∇d, plays a critical role in the subsequent modeling of crack propagation. Assuming a *given sharp crack surface topology* $\Gamma(t) \subset \mathcal{R}^{\delta-1}$ inside the solid $\mathcal{B}$ at time t, as depicted in Fig. 2a, we obtain in analogy to Eq. (3) the regularized crack phase field $d(\boldsymbol{x}, t)$ on $\mathcal{B}$, visualized in Fig. 2b, from the minimization principle

$$d(\boldsymbol{x}, t) = \text{Arg}\left\{ \inf_{d\in W_{\Gamma(t)}} \Gamma_l(d) \right\} \tag{8}$$

subject to the Dirichlet-type constraints $W_{\Gamma(t)} = \{d | d(\boldsymbol{x}, t) = 1 \text{ at } \boldsymbol{x} \in \Gamma(t)\}$. The Euler equations of the above variational principle are

$$d - l^2 \Delta d = 0 \text{ in } \mathcal{B} \quad \text{and} \quad \nabla d \cdot \boldsymbol{n} = 0 \text{ on } \partial\mathcal{B}, \tag{9}$$

where Δd is the Laplacian of the phase field and $\boldsymbol{n}$ the outward normal on $\partial\mathcal{B}$. Fig. 3 depicts a numerical solution of the *variational problem* (8) *of diffusive crack topology* and demonstrates the influence of the length scale l. We refer to the recent work Miehe, Welschinger & Hofacker [12], for a more detailed derivation.[1]

3. A framework of rate-independent diffusive fracture

With the idea of a diffusive crack topology at hand, we develop in this section a constitutive framework of phase-field-type fracture for the rate-independent setting. The subsequent formulation in terms of a history field is motivated in Appendix A by a simple one-dimensional structure of *local* damage mechanics. Fig. 4 provides a visual guide to the subsequent developments.

3.1. Degrading strain energy functional due to fracture

3.1.1. Displacement and strain fields

In the small-strain context, we describe the response of the fracturing solid by the *displacement field*

$$\boldsymbol{u} : \begin{cases} \mathcal{B}\times\mathcal{T} \to \mathcal{R}^\delta \\ (\boldsymbol{x}, t) \mapsto \boldsymbol{u}(\boldsymbol{x}, t) \end{cases} \tag{10}$$

in addition to the phase field d introduced in Eq. (5). $\boldsymbol{u}(\boldsymbol{x}, t) \in \mathcal{R}^\delta$ is the displacement of the material point $\boldsymbol{x} \in \mathcal{B}$ at time $t \in \mathcal{T}$. The strains are assumed to be small. Thus, the norm of the macroscopic displacement

[1] **Convergence to Sharp Crack Discontinuities**. The Γ–limit $\Gamma_l \to \Gamma$ of the functional Eq. (6) for vanishing length scale $l \to 0$ to the *sharp crack surface* $\Gamma := \int_\Gamma dA$ is considered in Braides [12], see Fig. 3 for a visualization. The functional Eq. (4) provides the basis for an elliptic regularization of the free discontinuity problem of brittle fracture. It has already been used in Bourdin, Francfort and Marigo [8] for the definition of a regularized surface energy. In contrast, we introduce the functional in the purely geometric context with regard to the subsequent definition of a dissipation potential.

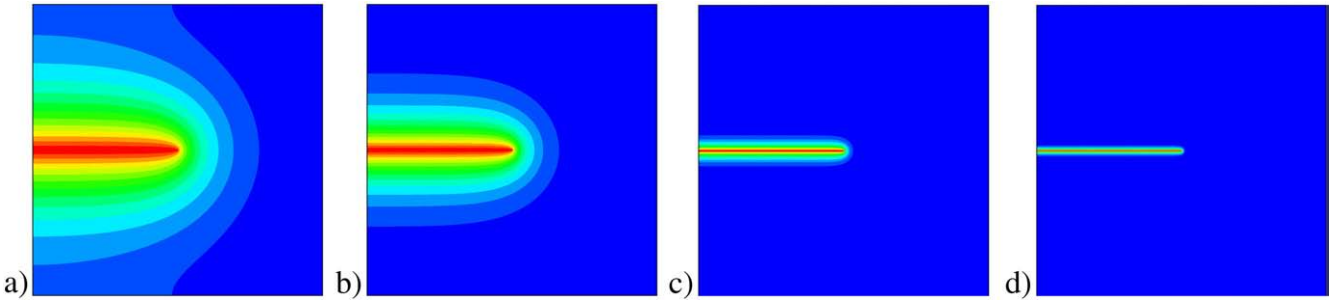

Fig. 3. Solutions of the variational problem (8) of diffusive crack topology for a quadratic specimen with a horizontal sharp crack Γ, taken from [1]. Regularized crack surfaces $\Gamma_l(d)$ governed by the crack phase field d for different length scales $l_a > l_b > l_c > l_d$. The sequence of pictures visualizes the Γ-limit $\Gamma_l \to \Gamma$ of the crack surface functional Eq. (6).

gradient $\|\nabla \boldsymbol{u}\| < \epsilon$ is bounded by a small number ϵ. The displacement gradient defines the small strain tensor

$$\boldsymbol{\varepsilon}(\boldsymbol{u}) = \nabla_s \boldsymbol{u} := \frac{1}{2}[\nabla \boldsymbol{u} + \nabla^T \boldsymbol{u}]. \tag{11}$$

In order to account for a stress degradation only in tension, we decompose the strain tensor into positive and negative parts

$$\boldsymbol{\varepsilon} = \boldsymbol{\varepsilon}_+ + \boldsymbol{\varepsilon}_- \tag{12}$$

describing tensile and compressive modes. These contributions are defined based on the spectral decomposition of the strain tensor $\boldsymbol{\varepsilon} = \sum_{i=1}^{\delta} \varepsilon^i \boldsymbol{n}^i \otimes \boldsymbol{n}^i$, where $\{\varepsilon^i\}_{i=1\ldots\delta}$ are the principal strains and $\{\boldsymbol{n}^i\}_{i=1\ldots\delta}$ the principal strain directions. We set

$$\boldsymbol{\varepsilon}_+ := \sum_{i=1}^{\delta} \langle \varepsilon^i \rangle_+ \boldsymbol{n}^i \otimes \boldsymbol{n}^i \quad \text{and} \quad \boldsymbol{\varepsilon}_- := \sum_{i=1}^{\delta} \langle \varepsilon^i \rangle_- \boldsymbol{n}^i \otimes \boldsymbol{n}^i \tag{13}$$

in terms of the bracket operators $\langle x \rangle_+ := (x + |x|)/2$ and $\langle x \rangle_- := (x - |x|)/2$, respectively. The derivative of Eq. (12) with respect to the total strains defines the two projection tensors

$$\mathbb{P}^+ := \partial_{\boldsymbol{\varepsilon}}[\boldsymbol{\varepsilon}_+(\boldsymbol{\varepsilon})] \quad \text{and} \quad \mathbb{P}^- := \mathbb{I} - \mathbb{P}^+, \tag{14}$$

which are isotropic tensor functions of $\boldsymbol{\varepsilon}$. These fourth-order tensors project the total strains onto its positive and negative parts, i.e. $\boldsymbol{\varepsilon}_+ = \mathbb{P}^+ : \boldsymbol{\varepsilon}$ and $\boldsymbol{\varepsilon}_- = \mathbb{P}^- : \boldsymbol{\varepsilon}$. The computation of these objects is performed by the algorithms outlined in Miehe [25] and Miehe & Lambrecht [26].

3.1.2. Constitutive free energy functional

We focus on the standard linear theory of elasticity for isotropic solids by considering the global energy storage functional

$$E(\boldsymbol{u}, d) = \int_{\mathcal{B}} \psi(\boldsymbol{\varepsilon}(\boldsymbol{u}), d) dV \tag{15}$$

that depends on the displacement $\boldsymbol{u}$ and the fracture phase field d. The *energy storage function* ψ describes the energy stored in the bulk of the solid per unit volume. A fully isotropic constitutive assumption for the degradation of energy due to fracture may have the form

$$\boxed{\psi(\boldsymbol{\varepsilon}, d) = [g(d) + k]\psi_0^+(\boldsymbol{\varepsilon}) + \psi_0^-(\boldsymbol{\varepsilon}).} \tag{16}$$

In this multiplicative ansatz, ψ_0 is an isotropic *reference energy function* associated with the undamaged elastic solid, i.e.

$$\psi_0(\boldsymbol{\varepsilon}) = \lambda \mathrm{tr}^2[\boldsymbol{\varepsilon}]/2 + \mu \mathrm{tr}[\boldsymbol{\varepsilon}^2] \tag{17}$$

with elastic constants $\lambda > 0$ and $\mu > 0$, which we additively decompose

$$\psi(\boldsymbol{\varepsilon}) = \psi_0^+(\boldsymbol{\varepsilon}) + \psi_0^-(\boldsymbol{\varepsilon}) \tag{18}$$

into a positive part ψ_0^+ due to tension and a negative part ψ_0^- due to compression. Here, we assume the definitions

$$\psi_0^+(\boldsymbol{\varepsilon}) = \lambda \langle \mathrm{tr}[\boldsymbol{\varepsilon}] \rangle_+^2 / 2 + \mu \mathrm{tr}[\boldsymbol{\varepsilon}_+^2] \quad \text{and} \quad \psi_0^-(\boldsymbol{\varepsilon}) = \lambda \langle \mathrm{tr}[\boldsymbol{\varepsilon}] \rangle_-^2 / 2 + \mu \mathrm{tr}[\boldsymbol{\varepsilon}_-^2] \tag{19}$$

with the above definitions of the brackets $\langle x \rangle_+$ and $\langle x \rangle_-$ and the positive and negative strain tensors $\boldsymbol{\varepsilon}_+$ and $\boldsymbol{\varepsilon}_-$, respectively. Note that both terms are positive. Furthermore, observe that the volumetric

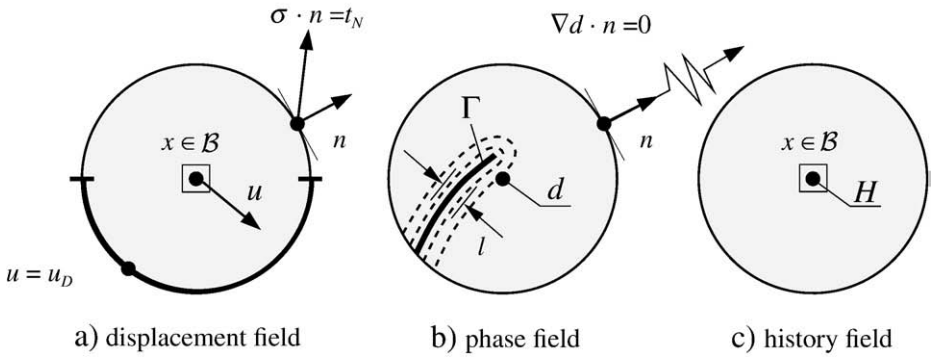

Fig. 4. A multi-field approach of phase-field-type crack propagation in deformable solids. The displacement field $\boldsymbol{u}$, the fracture phase field d and the history field $\mathcal{H}$ are defined on the solid domain $\mathcal{B}$. a) The displacement field is constrained by the Dirichlet- and Neumann-type boundary conditions $\boldsymbol{u} = \boldsymbol{u}_D$ on $\partial\mathcal{B}_u$ and $\boldsymbol{\sigma} \cdot \boldsymbol{n} = \boldsymbol{t}_N$ on $\partial\mathcal{B}_t$ with $\partial\mathcal{B} = \partial\mathcal{B}_u \cup \partial\mathcal{B}_t$. b) The fracture phase field is constrained by the possible Dirichlet-type boundary condition $d = 1$ on Γ and the Neumann condition $\nabla d \cdot \boldsymbol{n} = 0$ on the full surface $\partial\mathcal{B}$. c) The history field $\mathcal{H}$ defined in Eq. (40) contains a maximum *local strain energy* obtained within the fracture process. It drives the evolution of the fracture phase field d via Eq. (41).

Box 1
Staggered Scheme for Phase Field Fracture in $[t_n, t_{n+1}]$.

1. *Initialization.* The displacement, fracture phase and history fields $\boldsymbol{u}_n$, d_n and $\mathcal{H}_n$ at time t_n are known. Update prescribed loads $\bar{\boldsymbol{\gamma}}$, $\bar{\boldsymbol{u}}$, $\bar{\boldsymbol{t}}$ at current time t_{n+1}.
2. *Compute History.* Determine maximum reference energy obtained in history

$$\mathcal{H} = \begin{cases} \psi_0^+(\nabla_s \boldsymbol{u}_n) & \text{for } \psi_0^+(\nabla_s \boldsymbol{u}_n) > \mathcal{H}_n \\ \mathcal{H}_n & \text{otherwise} \end{cases}$$

in the domain $\mathcal{B}$ and store it as a history variable field.
3. *Compute Fracture Phase Field.* Determine the current fracture phase field d from the *minimization problem of crack topology*

$$d = \operatorname{Arg}\inf_d \left\{ \int_{\mathcal{B}} \left[g_c \gamma(d, \nabla d) + \frac{\eta}{2\tau}(d - d_n)^2 - (1-d)^2 \mathcal{H} \right] dV \right\}$$

with the crack surface density function

$$\gamma(d, \nabla d) = \frac{1}{2l} d^2 + \frac{l}{2} |\nabla d|^2.$$

4. *Compute Displacement Field.* Determine the current displacement $\boldsymbol{u}$ at frozen fracture phase field d from the *minimization problem of elasticity*

$$\boldsymbol{u} = \operatorname{Arg}\inf_{\boldsymbol{u}} \left\{ \int_{\mathcal{B}} [\psi(\nabla_s \boldsymbol{u}, d) - \bar{\boldsymbol{\gamma}} \cdot \boldsymbol{u}] dV - \int_{\partial \mathcal{B}_t} \bar{\boldsymbol{t}} \cdot \boldsymbol{u} dA \right\}$$

with the free energy density function

$$\psi(\boldsymbol{\varepsilon}, d) = [(1-d)^2 + k]\psi_0^+(\boldsymbol{\varepsilon}) + \psi_0^-(\boldsymbol{\varepsilon})$$

with $\psi_0^{\pm}(\boldsymbol{\varepsilon}) = \lambda \langle \operatorname{tr}[\boldsymbol{\varepsilon}] \rangle_{\pm}^2 / 2 + \mu \operatorname{tr}[\boldsymbol{\varepsilon}_{\pm}^2]$ for the Dirichlet-type boundary condition $\boldsymbol{u} = \bar{\boldsymbol{u}}$ on $\partial \mathcal{B}_u$.

contribution is chosen either positive or negative according to the sign of the volume dilatation $e = \operatorname{tr}[\boldsymbol{\varepsilon}]$, which cannot be expressed in terms of the positive and negative strain tensors $\boldsymbol{\varepsilon}_+$ and $\boldsymbol{\varepsilon}_-$. The monotonically decreasing *degradation function g(d)* describes the degradation of the positive (tensile) part of the stored energy with evolving damage. It is assumed to have the properties

$$g(0) = 1 \quad , \quad g(1) = 0 \quad , \quad g'(1) = 0. \tag{20}$$

The first two conditions include the limits for the unbroken and the fully-broken case. As shown below, the latter constraint ensures that the energetic fracture force converges to a finite value if the damage converges to the fully-broken state $d = 1$. A simple function that has the above properties is

$$g(d) = (1-d)^2. \tag{21}$$

The small positive parameter $k \approx 0$ in Eq. (16) circumvents the full degradation of the energy by leaving the *artificial elastic rest energy density* $k\psi_0(\boldsymbol{\varepsilon})$ at a fully-broken state $d = 1$. It is chosen as small as possible such that the algebraic conditioning number of the applied numerical discretization method remains well-posed for partly-broken systems.

3.1.3. Rate of energy functional

Taking the time derivative of Eq. (15), we obtain the *rate of energy* which we consider to be a functional of the rates $\{\dot{\boldsymbol{u}}, \dot{d}\}$

$$\dot{E}(\dot{\boldsymbol{u}}, \dot{d}; \boldsymbol{u}, d) = \int_{\mathcal{B}} [\boldsymbol{\sigma} : \nabla_s \dot{\boldsymbol{u}} - f \dot{d}] dV \tag{22}$$

at given state $\{\boldsymbol{u}, d\}$. Here, we introduced per definition the stress tensor

$$\boldsymbol{\sigma} := \partial_{\boldsymbol{\varepsilon}} \psi(\boldsymbol{\varepsilon}, d) = [(1-d)^2 + k][\lambda \langle \operatorname{tr}[\boldsymbol{\varepsilon}] \rangle_+ \boldsymbol{1} + 2\mu \boldsymbol{\varepsilon}_+] + [\lambda \langle \operatorname{tr}[\boldsymbol{\varepsilon}] \rangle_- \boldsymbol{1} + 2\mu \boldsymbol{\varepsilon}_-] \tag{23}$$

and the energetic force

$$f := -\partial_d \psi(\boldsymbol{\varepsilon}, d) = 2(1-d)\psi_0^+(\boldsymbol{\varepsilon}). \tag{24}$$

Note that the energetic force f is positive and bounded by a finite value for the limit $\psi_0^+(\boldsymbol{\varepsilon}) \to \infty$. As shown below this property ensures that the phase field variable is bounded by its maximum value $d = 1$. The key term that drives the crack evolution is the positive part $\psi_0^+(\boldsymbol{\varepsilon})$ of the reference energy, that may be considered to describe locally the intensity of the tensile part of the deformation.

3.2. Dissipation functional due to fracture

3.2.1. Dissipation due to crack propagation

For a given fracture surface functional $\Gamma(d)$ introduced in Eq. (6), we define the work needed to create a diffusive fracture topology by

$$W_c(d) := \int_{\mathcal{B}} g_c \gamma(d, \nabla d) dV, \tag{25}$$

where g_c is the Griffith-type critical energy release rate and $\gamma(d, \nabla d)$ the crack surface density function defined in Eq. (7). The rate of the work functional W_c defines the *crack dissipation*

$$\dot{W}_c(\dot{d}; d) = \int_{\mathcal{B}} (g_c \delta_d \gamma) \dot{d} dV, \tag{26}$$

which is considered to be a functional of the rate $\{\dot{d}\}$ of the crack phase field at given state $\{d\}$. Here, we introduced the variational or functional derivative

$$\delta_d\gamma(d) := \partial_d\gamma - \mathrm{Div}[\partial_{\nabla d}\gamma] = \frac{1}{l}[d - l^2\Delta d] \tag{27}$$

of the crack density function. Based on thermodynamical arguments, we demand

$$\dot{W}_c(\dot{d};d) \geq 0 \tag{28}$$

as the basic ingredient of our framework, enforcing a growth of the fracture work W_c defined in Eq. (25). Observe that we may satisfy this global irreversibility constraint of crack evolution by ensuring *locally* a positive variational derivative of the crack surface function and a positive evolution of the crack phase field

$$\delta_d\gamma \geq 0 \quad \text{and} \quad \dot{d} \geq 0. \tag{29}$$

The former condition is ensured in the subsequent treatment by a constitutive assumption that relates the functional derivative to a positive energetic driving force. The latter constraint is a natural assumption that relates the fracture phase field for the non-reversible evolution of micro-cracks and micro-voids.

3.2.2. Rate-independent evolution of the phase field

In order to satisfy the local constraints Eq. (29) within a possibly discontinuous, rate-independent evolution, we introduce the local threshold function

$$t_c(\beta;d) = \beta - g_c\delta_d\gamma(d) \leq 0 \tag{30}$$

formulated in terms of the variable β dual to d, in what follows denoted as the *driving force field*. Then, as shown below, the above local constraints Eq. (29) can be satisfied by the definition

$$\dot{W}_c(\dot{d};d) = \sup_{\beta,\lambda\geq 0} D_\lambda(\dot{d},\beta,\lambda;d) \tag{31}$$

in terms of the extended dissipation functional

$$D_\lambda(\dot{d},\beta,\lambda;d) = \int_{\mathcal{B}} [\beta\dot{d} - \lambda t_c(\beta;d)]dV \tag{32}$$

that includes the threshold function (30). λ is a Lagrange multiplier field.

3.3. Incremental variational principle and governing equations

3.3.1. An incremental variational principle

With the rate of the energy functional Eq. (22) and the extended dissipation functional Eq. (32) at hand, we introduce the incremental potential

$$\Pi_\lambda(\dot{\boldsymbol{u}},\dot{d},\beta,\lambda;\boldsymbol{u},d) = \dot{E}(\dot{\boldsymbol{u}},\dot{d};\boldsymbol{u},d) + D_\lambda(\dot{d},\beta,\lambda;d) - P(\dot{\boldsymbol{u}}), \tag{33}$$

that balances the internal power $\dot{E} + D_\lambda$ with the power due to external loading

$$P(\dot{\boldsymbol{u}}) = \int_{\mathcal{B}} \bar{\boldsymbol{\gamma}}\cdot\dot{\boldsymbol{u}}dV + \int_{\partial\mathcal{B}_t} \bar{\boldsymbol{t}}\cdot\dot{\boldsymbol{u}}dA. \tag{34}$$

Here, $\bar{\boldsymbol{\gamma}}$ is a prescribed volume force in $\mathcal{B}$ and $\bar{\boldsymbol{t}}$ a surface traction on $\partial\mathcal{B}_t$. We then obtain the basic field equations of the problem from the argument of virtual power that we base on the variational statement

$$\{\dot{\boldsymbol{u}},\dot{d},\beta,\lambda\} = \mathrm{Arg}\{\operatorname*{stat}_{\dot{\boldsymbol{u}},\dot{d},\beta,\lambda\geq 0} \Pi_\lambda(\dot{\boldsymbol{u}},\dot{d},\beta,\lambda;\boldsymbol{u},d)\}. \tag{35}$$

The variation of the functional with respect to the four field variables, taking into account $\delta\dot{\boldsymbol{u}} = 0$ on $\partial\mathcal{B}_u$, yields the coupled field equations

$$\begin{array}{lll} (1): & \mathrm{Div}[\boldsymbol{\sigma}] + \bar{\boldsymbol{\gamma}} & = \boldsymbol{0}, \\ (2): & \beta - f & = 0, \\ (3): & \dot{d} - \lambda & = 0, \\ (4): & \lambda & \geq 0, \\ (5): & \beta - g_c\delta_d\gamma & \leq 0, \\ (6): & \lambda(\beta - g_c\delta_d\gamma) & = 0 \end{array} \tag{36}$$

in the domain $\mathcal{B}$ along with the boundary conditions

$$\boldsymbol{\sigma}\cdot\boldsymbol{n} = \bar{\boldsymbol{t}} \text{ on } \partial\mathcal{B}_t \quad \text{and} \quad \nabla d\cdot\boldsymbol{n} = 0 \text{ on } \partial\mathcal{B}. \tag{37}$$

Note that we have introduced per definition the stress tensor $\boldsymbol{\sigma}$ and the energetic force f defined in Eqs. (23) and (24). The last three equations in Eq. (36) are the Kuhn-Tucker-type equations associated with the optimization problem with inequality constraints. From Eq. $(36)_{2,3}$, elimination of $\beta = f$ and $\lambda = \dot{d}$ yields the reduced system

$$\begin{array}{lll} (1): & \mathrm{Div}[\boldsymbol{\sigma}] + \bar{\boldsymbol{\gamma}} & = \boldsymbol{0}, \\ (2): & \dot{d} & \geq 0, \\ (3): & f - g_c\delta_d\gamma & \leq 0, \\ (4): & \dot{d}(f - g_c\delta_d\gamma) & = 0. \end{array} \tag{38}$$

Note that Eq. $(38)_2$ satisfies explicitly the desired thermodynamic consistency condition $(29)_2$. The first condition $g_c\delta_d\gamma \geq 0$ in $(29)_1$ is also satisfied. This may be seen if the damage field is computed in the case of loading from Eq. $(38)_3$, which results into

$$g_c\delta_d\gamma := \frac{g_c}{l}[d - l^2\Delta d] = 2(1-d)\psi_0^+(\boldsymbol{\varepsilon}) \quad \text{for} \quad \dot{d} > 0. \tag{39}$$

Note that the right hand side is positive which proves the condition $(29)_1$. Thus the proposed model of rate-independent diffusive crack evolution is consistent with the thermodynamic axiom of positive dissipation. Note furthermore, that Eq. (39) has the desired property $d \to 1$ for $\psi_0^+(\boldsymbol{\varepsilon}) \to \infty$.

3.3.2. Compact history-field-based formulation

It is clear that the '*load term*' $\psi_0^+(\varepsilon)$ in Eq. (39) determines the amount of the phase field variable d. Hence, motivated by Eq. (A.7) of the local damage model outlined in Appendix A, we may introduce the *local history field* of maximum positive reference energy

$$\mathcal{H}(\boldsymbol{x},t) := \max_{s\in[0,t]} \psi_0^+(\boldsymbol{\varepsilon}(\boldsymbol{x},s)) \tag{40}$$

obtained in a typical, possibly cyclical loading process. Replacing ψ_0^+ in Eq. (39) by this field, we obtain the equation

$$\boxed{\frac{g_c}{l}\left[d - l^2\Delta d\right] = 2(1-d)\mathcal{H}} \tag{41}$$

which determines the phase field in the case of loading *and* unloading. Note that this equation equips the crack topology Eq. $(9)_1$ by the local *crack source* on the right hand side. With this notion at hand, the proposed fracture phase field model may be reduced to the compact system of only two equations

$$\begin{array}{lll} (1): & \mathrm{Div}[\boldsymbol{\sigma}(\boldsymbol{u},d)] + \bar{\boldsymbol{\gamma}} & = \boldsymbol{0}, \\ (2): & g_c\delta_d\gamma(d) - 2(1-d)\mathcal{H} & = 0, \end{array} \tag{42}$$

which determine the current displacement and phase fields $\boldsymbol{u}$ and d in terms of the definitions (23), (40), (19) and (27) for the stresses $\boldsymbol{\sigma}$,

the history field $\mathcal{H}$ of maximum reference energy ψ_0^+ and the variational derivative $\delta_d\gamma$ of the crack density function. This is considered to be the most simple representation of rate-independent diffusive fracture, associated with the multi-field scenario visualized in Fig. 4.

3.4. Viscous regularization of the rate-independent problem

As commented on in Section 5, a viscous regularization of the above rate-independent formulation may stabilize the numerical treatment. It can be formulated in terms of a variational principle based on the potential

$$\Pi_\eta(\dot{\boldsymbol{u}},\dot{d},\beta;\boldsymbol{u},d) = \dot{E}(\dot{\boldsymbol{u}},\dot{d};\boldsymbol{u},d) + D_\eta(\dot{d},\beta;d) - P(\dot{\boldsymbol{u}}), \tag{43}$$

that includes a modified extended dissipation functional

$$D_\eta(\dot{d},\beta;d) = \int_{\mathcal{B}} [\beta\dot{d} - \frac{1}{\eta}\langle t_c(\beta;d)\rangle_+^2]dV, \tag{44}$$

where $\eta \geq 0$ is a viscosity parameter. The modified variational principle

$$\{\dot{\boldsymbol{u}},\dot{d},\beta\} = \text{Arg}\{\operatorname*{stat}_{\dot{\boldsymbol{u}},\dot{d},\beta} \Pi_\eta(\dot{\boldsymbol{u}},\dot{d},\beta;\boldsymbol{u},d)\} \tag{45}$$

then results in the coupled set of local equations

$$\begin{aligned} &(1): \quad \text{Div}[\boldsymbol{\sigma}] + \bar{\boldsymbol{\gamma}} &&= \boldsymbol{0}, \\ &(2): \quad \dot{d} - \frac{1}{\eta}\langle f - g_c\delta_d\gamma\rangle_+ &&= 0, \end{aligned} \tag{46}$$

where the field β has been eliminated. Note that the evolution $\dot{d}$ of the phase field is now governed by a viscous equation governed by the '*over-force*' $\langle f - g_c\delta_d\gamma\rangle_+$. As a consequence, Eq. (41) may be recast into the viscous regularized format

$$\boxed{\frac{g_c}{l}\left[d - l^2\Delta d\right] + \eta\dot{d} = 2(1-d)\mathcal{H}} \tag{47}$$

again driven by the local history field $\mathcal{H}$ of maximum positive reference energy defined in Eq. (40). This equation equips the crack topology Eq. $(9)_1$ by the *viscous resistance term* on the left hand side and the *crack source term* on the right hand side. Thus the viscous regularization of the system (42) reads

$$\begin{aligned} &(1): \quad \text{Div}[\boldsymbol{\sigma}(\boldsymbol{u},d)] + \bar{\boldsymbol{\gamma}} &&= \boldsymbol{0}, \\ &(2): \quad g_c\delta_d\gamma(d) + \eta\dot{d} - 2(1-d)\mathcal{H} &&= 0. \end{aligned} \tag{48}$$

The model is thermodynamically consistent by satisfying the constraints

$$\delta_d\gamma + \eta\dot{d} \geq 0 \quad \text{and} \quad \dot{d} \geq 0, \tag{49}$$

which contain in addition to Eq. (29) a contribution to the dissipation due to the viscous resistance of the phase field evolution. Observe that the rate-independent case is recovered by simply setting $\eta = 0$. This feature is a very convenient ingredient of a robust numerical implementation.

4. Staggered solution of incremental multi-field problem

We construct in this section a robust solution procedure of the multi-field problem visualized in Fig. 4 based on convenient algorithmic operator splits of the evolution equations.

4.1. Staggered update scheme of time-discrete fields

4.1.1. Time-discrete fields

We now consider field variables at the discrete times 0, t_1, t_2, …, t_n, t_{n+1}, …, T of the process interval $[0, T]$. In order to advance the solution within a typical time step, we focus on the finite time increment $[t_n, t_{n+1}]$, where

$$\tau_{n+1} := t_{n+1} - t_n > 0 \tag{50}$$

denotes the step length. In the subsequent treatment, all field variables at time t_n are assumed to be *known*. The goal then is to determine the fields at time t_{n+1} based on variational principles valid for the time increment under consideration. In order to obtain a compact notation, we drop in what follows the subscript $n+1$ and consider all variables without subscript to be evaluated at time t_{n+1}. In particular, we write

$$\boldsymbol{u}(\boldsymbol{x}) := \boldsymbol{u}(\boldsymbol{x}, t_{n+1}) \quad \text{and} \quad d(\boldsymbol{x}) := d(\boldsymbol{x}, t_{n+1}) \tag{51}$$

for the displacement and fracture phase field at the current time t_{n+1} and

$$\boldsymbol{u}_n(\boldsymbol{x}) := \boldsymbol{u}(\boldsymbol{x}, t_n) \quad \text{and} \quad d_n(\boldsymbol{x}) := d(\boldsymbol{x}, t_n) \tag{52}$$

for the fields at time t_n. As a consequence, the rates of the displacement and the fracture phase field are considered to be *constant* in the time increment Eq. (50) under consideration, defined by $\dot{\boldsymbol{u}} = (\boldsymbol{u} - \boldsymbol{u}_n)/\tau$ and $\dot{d} := (d - d_n)/\tau$. Note that, due to the given fields at time t_n, the above rates associated with the time increment Eq. (50) are linear functions of the variables (Eq. (51)) at the current time t_{n+1}.

4.1.2. Update of history field

We consider an operator split algorithm within the typical time step $[t_n, t_{n+1}]$ that allows a staggered update of the fracture phase field and the displacement field. The central idea for an algorithmic decoupling of the coupled equations is an approximated formulation of the current history field $\mathcal{H} := \mathcal{H}(\boldsymbol{x}, t_{n+1})$ in terms of the displacement field $\boldsymbol{u}_n$ at time t_n defined in Eq. (52). Starting from the initial condition

$$\mathcal{H}_0 := \mathcal{H}(\boldsymbol{x}, t = t_0) = 0, \tag{53}$$

we assume the current value of maximum reference energy obtained in history to be determined by

$$\mathcal{H} = \begin{cases} \psi_0^+(\nabla_s\boldsymbol{u}_n) & \text{for } \psi_0^+(\nabla_s\boldsymbol{u}_n) > \mathcal{H}_n, \\ \mathcal{H}_n & \text{otherwise.} \end{cases} \tag{54}$$

As a consequence of this simple definition, the energy $\mathcal{H}$ that drives the current fracture phase field d at time t_{n+1} is in the case of damage loading dependent on the displacement $\boldsymbol{u}_n$ at time t_n. With this algorithmic definition at hand, we may define *two decoupled variational problems* which define the phase field d and the displacement $\boldsymbol{u}$ at the current time t_{n+1}.

4.1.3. Update of phase field

Considering the energetic history $\mathcal{H}$ defined in Eq. (54) to be *constant* in the time interval $[t_n, t_{n+1}]$, we introduce the algorithmic functional

$$\Pi_d^\tau(d) = \int_{\mathcal{B}} [g_c\gamma(d,\nabla d) + \frac{\eta}{2\tau}(d-d_n)^2 - (1-d)^2\mathcal{H}]dV \tag{55}$$

where γ is the crack surface density function introduced in Eq. (7). The current fracture phase field is then computed from the algorithmic variational problem

$$d = \text{Arg}\{\inf_d \Pi_d^\tau(d)\}. \tag{56}$$

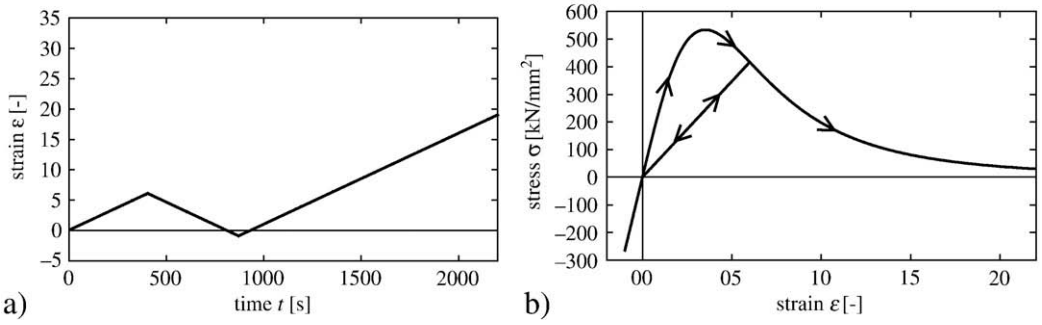

Fig. 5. Rate-independent local constitutive behavior. a) Cyclic driver in positive and negative range and b) stress response without damage evolution in compression.

The first two terms in the variational functional describe the crack surface resistance and the viscous resistance, respectively. The last term represents the source term governed by the energetic history field $\mathcal{H}$. Note that Π_d^τ is *quadratic*. Hence, the necessary condition of Eq. (56) is a simple linear problem for the determination of the current phase field. The Euler equation represents a discretized version of Eq. (47). Observe that the rate-independent case is recovered by simply setting the viscosity $\eta = 0$. This is considered as an important feature of our formulation. No ill-conditioning occurs for the limit $\eta = 0$. The viscosity is used as an artificial feature that stabilizes the simulation. It will be chosen as small as possible.

4.1.4. Update of displacement field

For a known fracture phase field d at time t_{n+1}, we compute the current displacement field $\boldsymbol{u}$ from the variational principle of linear elasticity. Let

$$\Pi_{\boldsymbol{u}}^\tau(\boldsymbol{u}) = \int_{\mathcal{B}} [\psi(\nabla_s \boldsymbol{u}; d) - \overline{\boldsymbol{\gamma}} \cdot \boldsymbol{u}] dV - \int_{\partial \mathcal{B}_t} \overline{\boldsymbol{t}} \cdot \boldsymbol{u} dA \tag{57}$$

be the elastic potential energy at given phase field d, we get the displacement field from the minimization problem

$$\boldsymbol{u} = \text{Arg}\{\inf_{\boldsymbol{u}} \Pi_{\boldsymbol{u}}^\tau(\boldsymbol{u})\} \tag{58}$$

of elasticity. Note that ψ is quadratic. Thus the necessary condition of Eq. (58) gives a linear system.

4.1.5. Staggered update scheme

The staggered algorithm in the time interval $[t_n, t_{n+1}]$ is summarized in Box 1. It represents a sequence of two linear subproblems for the successive update of the fracture phase field and the displacement field. Such an algorithm is extremely robust. Clearly, it may slightly underestimate the speed of the crack evolution when compared with a fully monolithic solution of the coupled problem as considered in Miehe, Welschinger & Hofacker [1]. However, this can be controlled by making use of an adaptive time stepping rule.

4.2. Spatial discretization of the staggered problem

Let $\mathfrak{T}^h$ denote a finite element triangulation of the solid domain $\mathcal{B}$. The index h indicates a typical mesh size based on E^h finite element domains $\mathcal{B}_e^h \in \mathfrak{T}^h$ and N^h global nodal points. We use the same triangulation for spatial discretization of both the phase field as well as the displacement field.

4.2.1. Update of phase field

Associated with $\mathfrak{T}^h$, we write the finite element interpolations of the phase field and its gradient by

$$\boldsymbol{c}_d^h := \{d, \nabla d\}^h = \boldsymbol{B}_d(\boldsymbol{x}) \boldsymbol{d}_d(t) \tag{59}$$

in terms of the nodal phase field vector $\boldsymbol{d}_d \in \mathcal{R}^{N^h}$. $\boldsymbol{B}_d$ is a symbolic representation of a global interpolation matrix, containing the shape functions and their derivatives.[2] Introducing the potential density function

$$\pi_d^\tau(d, \nabla d) = g_c \gamma(d, \nabla d) + \frac{\eta}{2}(d - d_n)^2 - (1-d)^2 \mathcal{H}, \tag{60}$$

in Eq. (55), the spatial discretization of the variational principle (56) reads

$$\boldsymbol{d}_d = \text{Arg}\left\{\inf_{\boldsymbol{d}_d} \int_{\mathcal{B}^h} \pi_d^\tau(\boldsymbol{B}_d \boldsymbol{d}_d) dV\right\}. \tag{61}$$

The associated Euler equation is linear and can be solved in closed form

$$\boldsymbol{d}_d = -\left[\int_{\mathcal{B}^h} \boldsymbol{B}_d^T [\partial^2_{\boldsymbol{c}_d \boldsymbol{c}_d} \pi_d^\tau] \boldsymbol{B}_d dV\right]^{-1} \int_{\mathcal{B}^h} \boldsymbol{B}_d^T [\partial_{\boldsymbol{c}_d} \pi_d^\tau] dV \tag{62}$$

for the current nodal values of the phase field at time t_{n+1}.

4.2.2. Update of displacement field

Associated with $\mathfrak{T}^h$, we write the finite element interpolations of the displacement field and its symmetric gradient by

$$\boldsymbol{c}_u^h := \{\boldsymbol{u}, \nabla_s \boldsymbol{u}\}^h = \boldsymbol{B}_u(\boldsymbol{x}) \boldsymbol{d}_u(t) \tag{63}$$

in terms of the nodal displacement vector $\boldsymbol{d}_u \in \mathcal{R}^{\delta N^h}$. The symbolic global interpolation matrix $\boldsymbol{B}_u$ contains the shape functions and its derivatives. Introducing the potential density function

$$\pi_u^\tau(\boldsymbol{u}, \nabla_s \boldsymbol{u}) = \psi(\nabla_s \boldsymbol{u}; d) - \overline{\boldsymbol{\gamma}} \cdot \boldsymbol{u}, \tag{64}$$

in Eq. (57), the spatial discretization of the variational principle (58) reads for a zero traction problem

$$\boldsymbol{d}_u = \text{Arg}\left\{\inf_{\boldsymbol{d}_u} \int_{\mathcal{B}^h} \pi_u^\tau(\boldsymbol{B}_u \boldsymbol{d}_u) dV\right\}. \tag{65}$$

[2] **Shapes of FE Discretization**. For two-dimensional plane strain problems $\delta = 2$, the constitutive state vector of the phase field discretization Eq. (59) reads $\boldsymbol{c}_d = [d, d_{,1}, d_{,2}]$. Then, associated with node I of a standard finite element e, the finite element interpolation matrix has the form

$$[\boldsymbol{B}_d]_I^e = \begin{bmatrix} N & N_{,1} & N_{,2} \end{bmatrix}_I^T$$

in terms of the shape function N_I at note I and their derivatives. The state vector of the displacement discretization reads $c_u = [u_1, u_2, u_{1,1}, u_{2,2}, u_{1,2} + u_{2,1}]$ and the associated finite element interpolation matrix has the form

$$[\boldsymbol{B}_u]_I^e = \begin{bmatrix} N & 0 & N_{,1} & 0 & N_{,2} \\ 0 & N & 0 & N_{,2} & N_{,1} \end{bmatrix}_I^T.$$

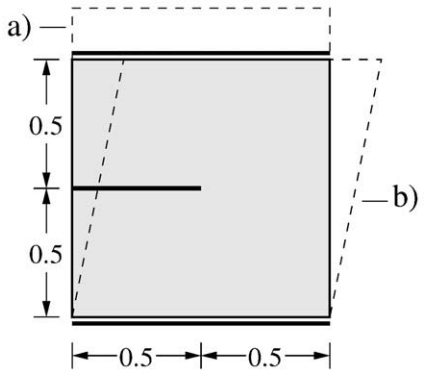

Fig. 6. Single edge notched specimen. Geometry and boundary conditions. a) Tension test treated in Section 5.1 and b) shear test treated in Section 5.2.

The associated Euler equation of linear elasticity yields the closed form solution

$$\boldsymbol{d}_u = -\Big[\int_{\mathcal{B}^h} \boldsymbol{B}_u^T[\partial^2_{\mathfrak{c}_u\mathfrak{c}_u}\pi_u^\tau]\boldsymbol{B}_u\,dV\Big]^{-1}\int_{\mathcal{B}^h}\boldsymbol{B}_u^T[\partial_{\mathfrak{c}_u}\pi_u^\tau]dV \tag{66}$$

for the current nodal values of the phase field at time t_{n+1}.

5. Representative numerical examples

We now demonstrate the modeling capability of the proposed approach to diffusive fracture by means of numerical model problems. The proposed staggered scheme outlined in Box 1 based on the local history field is much faster than the monolithic three-field formulation outlined in Miehe, Welschinger & Hofacker [1]. As shown below, it allows performing rate-independent problems in a straightforward manner. We demonstrate this for a spectrum of standard benchmark problems such as a single edge notched specimen subjected to tensile and pure shear loadings, a symmetric and an asymmetric notched three point bending test. The characteristic of the *local material response* for a cyclic loading process is demonstrated in Fig. 5. The result is obtained by a local driving of the constitutive model. It shows the basic properties of a rate-independent hysteresis due to local damage mechanisms which occur only in the tensile range. There is no diffusive fracture evolution in the compressive range.

5.1. Single edge notched tension test

Consider a squared plate with horizontal notch which is placed at middle height from the left outer surface to the center of the specimen. The geometric setup is depicted in Fig. 6. In order to capture

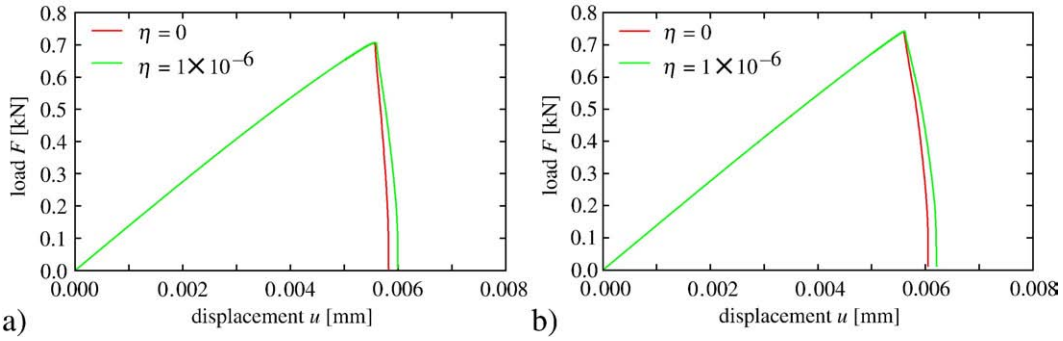

Fig. 7. Single edge notched tension test. Load-deflection curves for a length scale a) $l_1 = 0.0150$ mm and b) $l_2 = 0.0075$ mm obtained for $\eta = 1\times10^{-6}$ kN s/mm^2 and $\eta = 0$ kN s/mm^2.

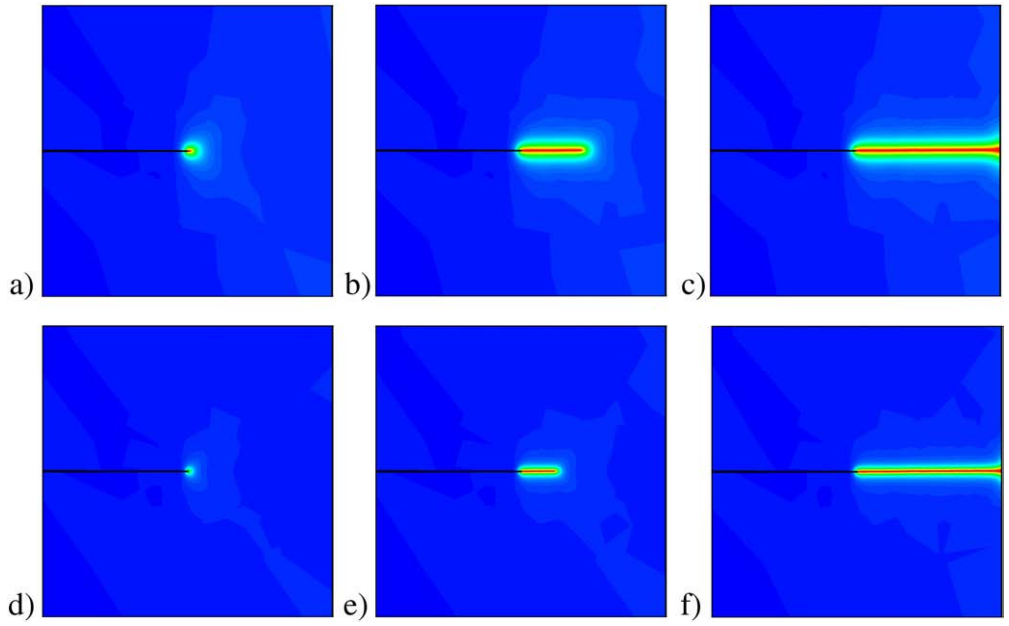

Fig. 8. Single edge notched tension test. Crack pattern for $\eta = 1\times10^{-6}$ kN s/mm^2 at a displacement of a) $u = 5.7\times10^{-3}$ mm, b) $u = 5.9\times10^{-3}$ mm, c) $u = 6.1\times10^{-3}$ mm for a length scale of $l_1 = 0.0150$ mm and d) $u = 5.7\times10^{-3}$ mm, e) $u = 5.9\times10^{-3}$ mm, and f) $u = 6.3\times10^{-3}$ mm for a length scale of $l_2 = 0.0075$ mm.

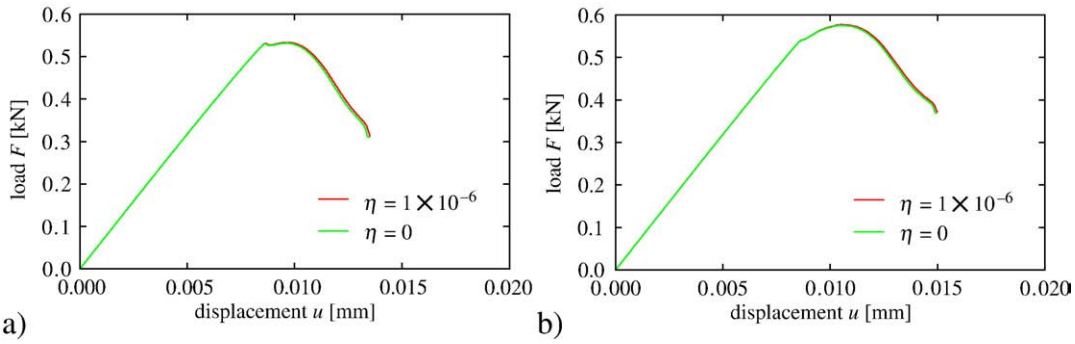

Fig. 9. Single edge notched pure shear test. Load-deflection curves for a length scale a) $l_1 = 0.0150$ mm and b) $l_2 = 0.0075$ mm obtained for $\eta = 1 \times 10^{-6}$ kN s/mm^2 and $\eta = 0$ kN s/mm^2.

the crack pattern properly, the mesh is refined in areas where the crack is expected to propagate, i.e. in the centered strip of the specimen. For a discretization with 20,000 elements an effective element size of $h \approx 0.001$ mm in the critical zone is obtained. Following [1], we choose the maximum element size in this zone to be one half of the length scale. The elastic bulk modulus is chosen to $\lambda = 121.15$ kN/mm^2, the shear modulus to $\mu = 80.77$ kN/mm^2 and the critical energy release rate to $g_c = 2.7 \times 10^{-3}$ kN/mm. The computation is performed in a monotonic displacement driven context with constant displacement increments of $\Delta u = 1 \times 10^{-5}$ mm in the first 500 time steps and needs to be adjusted to $\Delta u = 1 \times 10^{-6}$ mm in the remaining time steps due to the brutal character of the crack propagation. In order to point out the effects which arise due to the length scale parameter l and a viscosity η, different simulations are performed. For fixed length scale parameters $l_1 = 0.0150$ mm and $l_2 = 0.0075$ mm, the influence of the viscosity is analyzed. The load-deflection curves obtained are depicted in Fig. 7. One observes that for the *rate-independent case* $\eta = 0$ the structural response shows a steeper descent whereas the viscous model smoothes out the brutal crack propagation in the post critical regime. The results are in agreement with a monolithic solution, see Fig. 12 in Miehe, Welschinger & Hofacker [1]. As expected, the sharpest crack pattern is obtained for the smallest length scale parameter $l_2 = 0.0075$ mm. The resulting crack patterns at different stages of the deformation for the length scales $l_1 = 0.0150$ mm and $l_2 = 0.0075$ mm are illustrated in Fig. 8. The illustration uses the viscous model with $\eta = 1 \times 10^{-6}$ kN s/mm^2, which does not show the brutal crack evolution of the rate-independent problem. The viscosity has a stabilizing effect. However, we are able to compute the rate-independent limit without problems.

5.2. Single edge notched pure shear test

We now investigate the same squared plate with horizontal notch as in the previous example for a shear loading mode. The geometric setup and the applied deformation are depicted in Fig. 6. In order to capture the crack pattern properly, the mesh is again refined in areas where the crack is expected to propagate, i.e. in the lower right diagonal strip of the specimen. An effective element size of approximately $h \approx 0.002$ mm

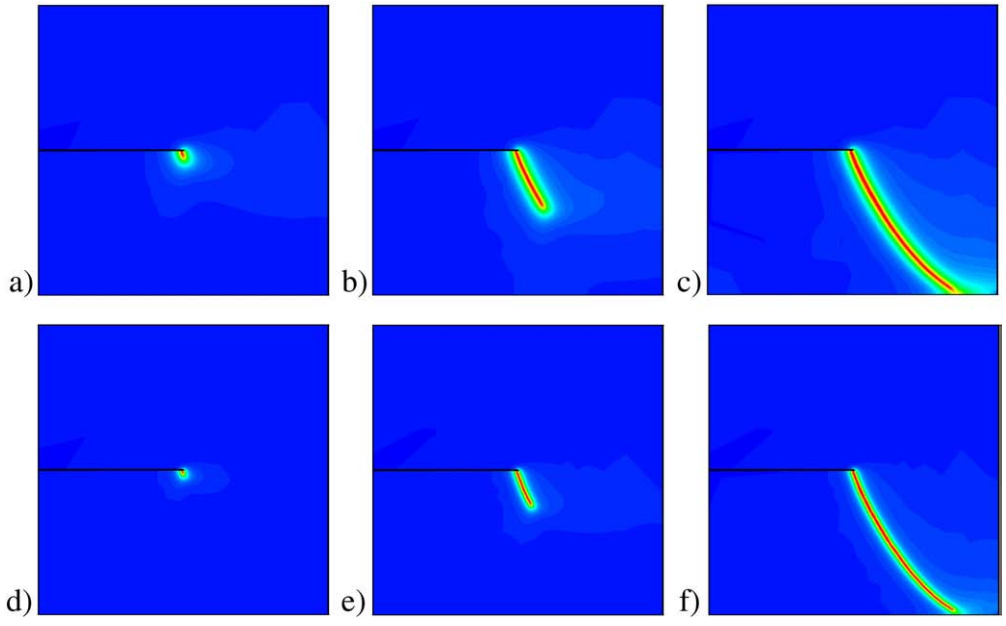

Fig. 10. Single edge notched pure shear test. Crack pattern for $\eta = 1 \times 10^{-6}$ kN s/mm^2 at a displacement of a) $u = 9.0 \times 10^{-3}$ mm, b) $u = 11.0 \times 10^{-3}$ mm, c) $u = 13.4 \times 10^{-3}$ mm for a length scale of $l_1 = 0.0150$ mm and d) $u = 9.0 \times 10^{-3}$ mm, e) $u = 11.0 \times 10^{-3}$ mm, and f) $u = 14.8 \times 10^{-3}$ mm for a length scale of $l_2 = 0.0075$ mm.

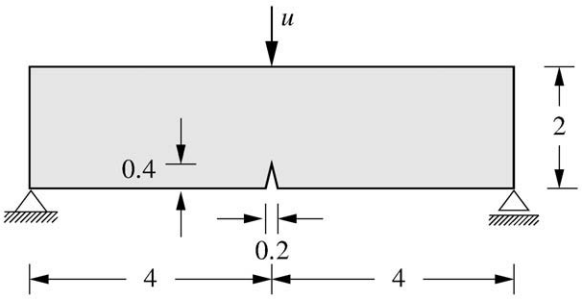

Fig. 11. Symmetric three point bending test. Geometry and boundary conditions.

based on a mesh with 30,000 elements is used. The elastic bulk modulus is chosen to $\lambda = 121.15$ kN/mm^2, the shear modulus to $\mu = 80.77$ kN/mm^2 and the critical energy release rate to $g_c = 2.7 \times 10^{-3}$ kN/mm. The computation is performed in a monotonic displacement driven context with constant displacement increments of $\Delta u = 1 \times 10^{-5}$ mm. Again, we perform different simulations in order to point out the effects due to different length scale parameters l and viscosity η. For fixed length scale parameters $l_1 = 0.0150$ mm and $l_2 = 0.0075$ mm, the influence of the viscosity is analyzed. The load–deflection curves obtained are depicted in Fig. 9. For the *rate-independent case* $\eta = 0$ the structural response shows a steeper descent whereas the viscous model smoothes out the brutal crack propagation in the post critical range. As expected, the sharpest crack pattern is obtained for the smallest length scale parameter $l_2 = 0.0075$ mm. The resulting crack patterns at different stages of the deformation for the length scales $l_1 = 0.0150$ mm and $l_2 = 0.0075$ mm are illustrated in Fig. 10.

5.3. Symmetric three point bending test

This test is a classical benchmark problem which has often been analyzed in literature, for example in the recent work Miehe & Gürses [20] in the context of configurational-force-driven crack propagation: a simply supported notched beam. The geometric setup as well as the loading conditions are illustrated in Fig. 11. The discretization is refined in the expected crack propagation zone, yielding a discretization with 20,000 elements and an effective element size of $h \approx 0.0008$ mm in the critical zone. The bulk modulus is chosen to $\lambda = 12.00$ kN/mm^2, the shear modulus to $\mu = 8.0$ kN/mm^2 and the critical energy release rate to $g_c = 5.0 \times 10^{-4}$ kN/mm. The computation is performed in a monotonic displacement driven context with constant displacement increments $\Delta u = 1 \times 10^{-4}$ mm in the first 360 loading steps. Continuing crack propagation then demands for an adjustment of the displacement increment to $\Delta u = 1 \times 10^{-6}$ mm for the subsequent loading steps. Fig. 12 illustrates the global response for two different length scales in combination with different viscosities. In Fig. 12a results for a length scale $l_1 = 0.06$ mm and in Fig. 12b for a length scale $l_2 = 0.03$ mm are compared to a simulation obtained from a fracture model based on configurational-force-driven crack propagation introduced by Miehe & Gürses [20] for a simulation with 10,360 elements. The proposed new phase field model shows a very good agreement even for the use of larger length scales. The resulting contour plots of the crack topology, again for the two different length scale parameters under focus, are given in Fig. 13. Blue and red colors correspond to the undamaged and the fully cracked material, respectively. In summary, we emphasis that the proposed phase field model of fracture yields a very good agreement with results

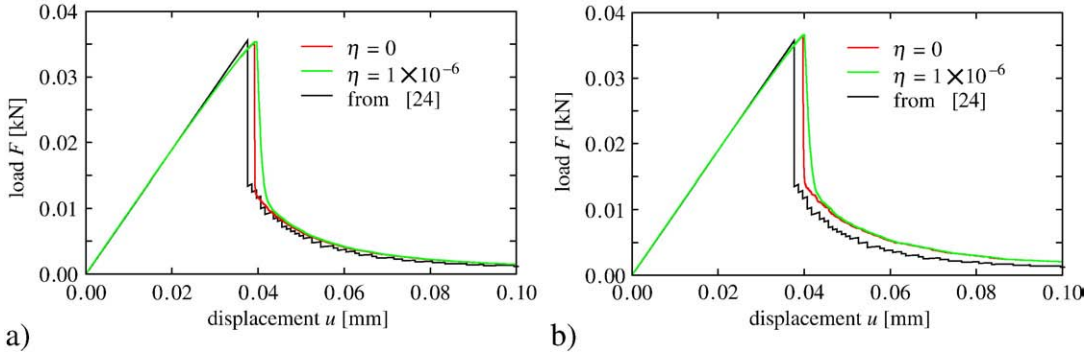

Fig. 12. Symmetric three point bending test. Load-deflection curves for a length scale a) $l_1 = 0.06$ mm and b) $l_2 = 0.03$ mm obtained for $\eta = 1 \times 10^{-6}$ kN s/mm^2 and $\eta = 0$ kN s/mm^2. Structural response is compared to the material force based algorithm, see Miehe et al. [24].

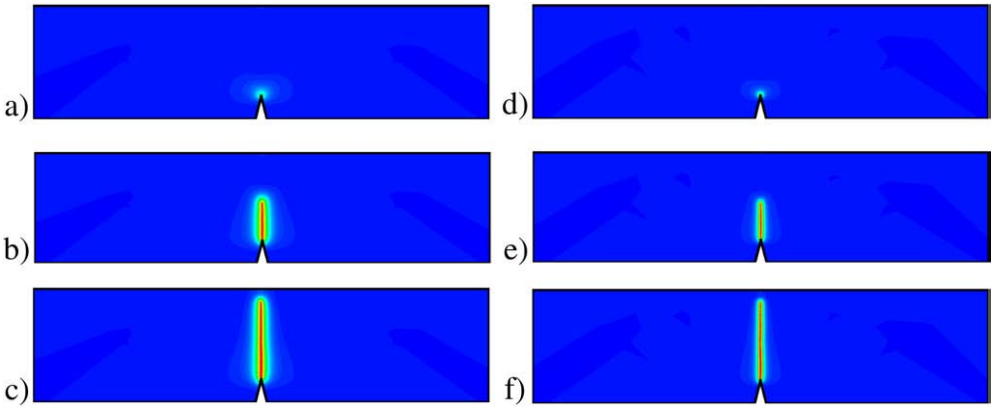

Fig. 13. Symmetric three point bending test. Crack pattern for $\eta = 0$ kN s/mm^2 at a displacement of a) $u = 4.0 \times 10^{-2}$ mm, b) $u = 4.1 \times 10^{-2}$ mm, c) $u = 1.0 \times 10^{-1}$ mm for a length scale of $l_1 = 0.06$ mm and d) $u = 3.8 \times 10^{-2}$ mm, e) $u = 4.1 \times 10^{-2}$ mm, and f) $u = 1.0 \times 10^{-1}$ mm for a length scale of $l_2 = 0.03$ mm.

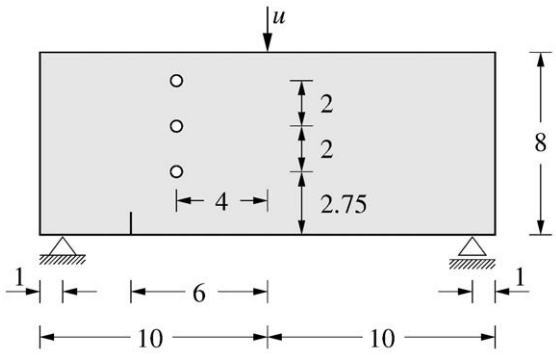

Fig. 14. Asymmetric notched three point bending test. Geometry, loading and boundary conditions from Bittencourt et al. [27]. The three holes have a diameter of 0.5.

obtained by alternative computational methods of rate-independent brittle fracture.

5.4. Asymmetric notched three point bending test

Next, we apply the rate-independent fracture model to a more complex boundary value problem with an evolving curvilinear crack trajectory.

The asymmetric three point bending test was analyzed experimentally and numerically in Bittencourt et al. [27]. It concerns an asymmetrically-notched beam with three holes. The setup of the problem is shown in Fig. 14. The material parameters are the elastic constants $\lambda = 12.00$ kN/mm^2, $\mu = 8.0$ kN/mm^2 and the critical energy release rate $g_c = 1 \times 10^{-3}$ kN/mm. The mesh consists of 58,000 triangular elements and is refined in areas where the crack is expected to propagate. The length scale parameter is chosen to $l = 0.025$ mm which is twice the element size. Fig. 15 illustrates the crack path obtained by different numerical models in comparison to the experimental result. The first two pictures show the crack path based on the rate-independent fracture model. In Fig. 15a and b the results are obtained for $\eta = 1.0 \times 10^{-6}$ kN s/mm^2 and $\eta = 0.0$ kN s/mm^2, respectively. Fig. 15c visualizes the crack path of the configurational force model analyzed in Miehe & Gürses [20]. Fig. 15d finally shows the experimental result of Bittencourt et al. [27]. Taking a closer look at the first two pictures, one can observe a slight difference regarding the width of the crack paths, although an equal length scale parameter was used for the simulation. This effect can be related to the brutal character of the crack propagation for zero viscosity. Adding a very small amount of viscosity improves the robustness. A comparison of the results obtained by the phase field model, the configurational force model and the experimental analysis shows that both strategies capture the experimentally observed curved crack pattern very well. The configurational force model with the adaptive reorientation of the segments at the crack tip yields crack trajectories for quite rough meshes. However, such a formulation is of limited applicability, because it cannot be applied to the modeling of crack initiation in solids free of defects and does not allow for crack branching. These problems are overcome by the proposed phase field model for fracture. The strong influence of the viscosity on curvilinear crack patterns in the phase field modeling of fracture has already been discussed in Miehe, Welschinger & Hofacker [1]. Hence, a key advantage of the algorithmic formulation proposed in this work is that robust computations can be performed for the full *rate-independent response* without any viscosity. Finally, Fig. 16 shows the evolution of the contour plots, again blue and red colors correspond to the undamaged and fully cracked states, respectively.

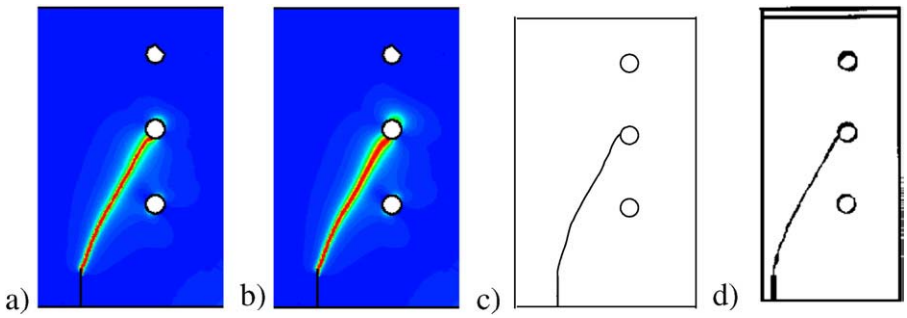

Fig. 15. Asymmetric notched three point bending test. Crack topology of the rate-independent formulation with 58,000 elements and a) a viscosity $\eta = 1.0 \times 10^{-6}$ kN s/mm^2 and b) a zero viscosity. c) Crack trajectories of Miehe & Guerses [20] and d) experimentally-obtained crack patterns by Bittencourt et al. [27].

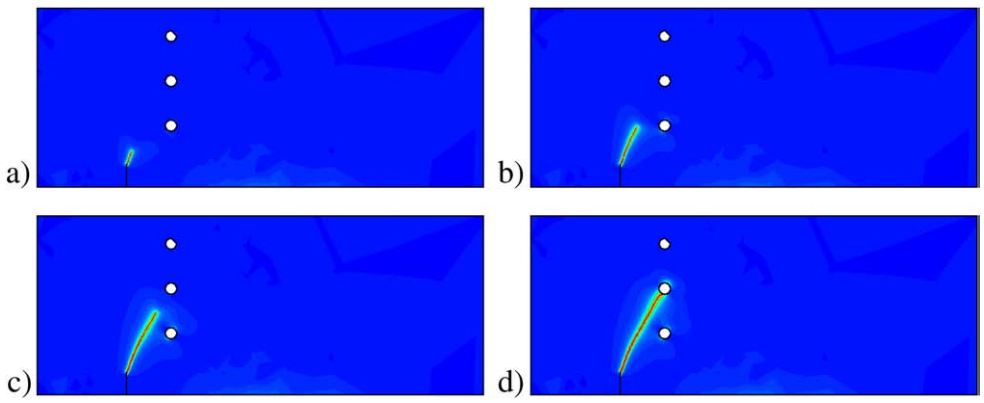

Fig. 16. Asymmetric notched three point bending test. a)–d) Crack pattern for $\eta = 1 \times 10^{-6}$ kN s/mm^2 at different stages of the deformation for a length scale of $l = 0.025$ mm.

6. Conclusion

We outlined a thermodynamically consistent framework for rate-independent diffusive crack propagation in elastic solids. To this end, we proposed a new incremental variational framework for rate-independent diffusive fracture that bases on the introduction of a local history field. It contains a maximum reference energy obtained in the deformation history, which may be considered as a measure for the maximum tensile strain obtained in history. It was shown that this local variable drives the evolution of the fracture phase field. It allowed the construction of an extremely robust operator split scheme that successively updates in a typical time step the history field, the crack phase field and finally the displacement field. An artificial viscous regularization stabilizes the overall performance. The proposed algorithm is considered to be the canonically simple scheme for the treatment of diffusive fracture. We demonstrated the performance of the proposed phase field formulations of fracture by means of representative numerical examples.

Acknowledgment

Support for this research was provided by the German Research Foundation (DFG) under grant Mi 295/11-2.

Appendix A. Introduction of a damage-driving history field

In order to motivate the structure of the diffusive fracture model outlined in Section 3, we consider a *local* damage model in a one-dimensional setting. It is governed by a free energy function

$$\psi(\varepsilon,d) = g(d)\psi_0(\varepsilon) \quad \text{with} \quad g(d) = (1-d)^2 \quad \text{and} \quad \psi_0(\varepsilon) = \tfrac{1}{2}E\varepsilon^2 \tag{A.1}$$

in terms of the convex reference energy function $\psi_0(\varepsilon)=\psi(\varepsilon,0)$ and the degrading function $g(d)$, which depend on the strain ε and the internal damage variable d. E is the elastic stiffness. The degrading function is positive $g\geq 0$, monotonic decreasing $g'\leq 0$ and has the properties $g(0)=1$, $g(1)=0$ and $g'(1)=0$. From Eq. (A.1), we obtain by a standard exploitation method of the second axiom of thermodynamics, often referred to as Coleman's method, the constitutive expression for the stresses

$$\sigma(\varepsilon,d) := \partial_\varepsilon\psi(\varepsilon,d) = (1-d)^2 E\varepsilon \tag{A.2}$$

and the reduced dissipation inequality

$$\mathcal{D} = f\dot{d} \geq 0 \quad \text{with} \quad f(\varepsilon,d) := -\partial_d\psi(\varepsilon,d) = 2(1-d)\psi_0(\varepsilon). \tag{A.3}$$

A rate-independent, discontinuous evolution of the internal variable can be based on the threshold function

$$t(f;d) = f - cd. \tag{A.4}$$

Here, the constant $c=1\ N/m^2$ has the value one and the unit of an energy density. With this function at hand, a rate-independent evolution of damage is defined by the equations

$$\dot{d} \geq 0, \quad t(f;d) \leq 0, \quad \dot{d}t(f;d) = 0. \tag{A.5}$$

Considering damage loading, $\dot{d}>0$, we may compute the current damage variable d from the condition $t(f;d)=0$ in Eq. $(71)_2$, yielding the closed form solution

$$d = \frac{h(\varepsilon)}{c + h(\varepsilon)} \quad \text{for} \quad \dot{d} > 0 \quad \text{with} \quad h(\varepsilon) = 2\psi_0(\varepsilon) = |\varepsilon|_E^2, \tag{A.6}$$

where the function $h(\varepsilon)$ is directly related to the reference energy $\psi_0(\varepsilon)$. As outlined in Eq. $(A.6)_3$, the convex reference free energy is a quadratic function of the norm $|\varepsilon|_E$ of the strain ε with regard to a metric provided by the elasticity modulus E. It obviously *drives* the accumulation of the damage variable d. Note that Eq. $(A.6)_1$ provides the desired property $d\to 1$ for $h(\varepsilon)\to\infty$ or $|\varepsilon|_E\to\infty$. Furthermore, observe that damage accumulation $\dot{d}>0$ takes place only if the function $h(\varepsilon)$ defined in Eq. $(A.6)_3$ *grows*. Defining $\mathcal{H}(t)$ as the maximum value of $h(\varepsilon(t))$ obtained in *time history*, we may replace system (A.5) for the rate-independent evolution of the damage variable d by the simple closed-form equation

$$d(t) = \frac{\mathcal{H}(t)}{c + H(t)} \quad \text{with} \quad \mathcal{H}(t) := max_{s\in[0,t]}\{h(\varepsilon(s))\}. \tag{A.7}$$

See for example Miehe [28] for an analogous definition of a history field in rate-independent, discontinuous damage mechanics. The two Eqs. (A.2) and (A.7) then govern exclusively a damage-type degrading stress response in an elastic solid. Note that in this model due to $E>0$ the current damage variable d is in a one-to-one relationship to the *maximum strain norm* obtained in time history

$$\varepsilon_{max}(t) := \max_{s\in[0,t]}\{\,|\varepsilon(s)|\,\} = \sqrt{\mathcal{H}(t)/E}. \tag{A.8}$$

References

[1] C. Miehe, F. Welschinger, M. Hofacker, Thermodynamically-consistent phase field models of fracture: Variational principles and multi-field fe implementations, International Journal for Numerical Methods in Engineering DOI: 10.1002/nme.2861.
[2] A.A. Griffith, The phenomena of rupture and flow in solids, Philosophical Transactions of the Royal Society London A 221 (1921) 163–198.
[3] G.R. Irwin, Fracture, in: S. Flügge (Ed.), Elasticity and Plasticity, Encyclopedia of Physics, Vol. 6, Springer, 1958, pp. 551–590.
[4] G.A. Francfort, J.J. Marigo, Revisiting brittle fracture as an energy minimization problem, Journal of the Mechanics and Physics of Solids 46 (1998) 1319–1342.
[5] B. Bourdin, G.A. Francfort, J.J. Marigo, The Variational Approach to Fracture, Springer Verlag, Berlin, 2008.
[6] G. Dal Maso, R. Toader, A model for the quasistatic growth of brittle fractures: Existence and approximation results, Archive for Rational Mechanics and Analysis 162 (2002) 101–135.
[7] M. Buliga, Energy minimizing brittle crack propagation, Journal of Elasticity 52 (1999) 201–238.
[8] B. Bourdin, G.A. Francfort, J.J. Marigo, Numerical experiments in revisited brittle fracture, Journal of the Mechanics and Physics of Solids 48 (2000) 797–826.
[9] D. Mumford, J. Shah, Optimal approximations by piecewise smooth functions and associated variational problems, Communications on Pure and Applied Mathematics 42 (1989) 577–685.
[10] L. Ambrosio, V.M. Tortorelli, Approximation of functionals depending on jumps by elliptic functionals via γ-convergence, Communications on Pure and Applied Mathematics 43 (1990) 999–1036.
[11] G. Dal Maso, An Introduction to Γ-Convergence, Birkhäuser, Boston, 1993.
[12] D.P. Braides, Approximation of Free Discontinuity Problems, Springer Verlag, Berlin, 1998.
[13] D.P. Braides, Γ-Convergence for Beginners, Oxford University Press, New York, 2002.
[14] V. Hakim, A. Karma, Laws of crack motion and phase-field models of fracture, Journal of the Mechanics and Physics of Solids 57 (2009) 342–368.
[15] A. Karma, D.A. Kessler, H. Levine, Phase-field model of mode iii dynamic fracture, Physical Review Letters 92 (2001) 8704.045501.
[16] L.O. Eastgate, J.P. Sethna, M. Rauscher, T. Cretegny, C.-S. Chen, C.R. Myers, Fracture in mode i using a conserved phase-field model, Physical Review E 65 (2002) 036117-1-10.
[17] T. Belytschko, H. Chen, J. Xu, G. Zi, Dynamic crack propagation based on loss of hyperbolicity and a new discontinuous enrichment, International Journal for Numerical Methods in Engineering 58 (2003) 1873–1905.
[18] J.-H. Song, T. Belytschko, Cracking node method for dynamic fracture with finite elements, International Journal for Numerical Methods in Engineering 77 (2009) 360–385.
[19] E. Gürses, C. Miehe, A computational framework of three-dimensional configurational-force-driven brittle crack propagation, Computer Methods in Applied Mechanics and Engineering 198 (2009) 1413–1428.
[20] C. Miehe, E. Gürses, A robust algorithm for configurational-force-driven brittle crack propagation with r-adaptive mesh alignment, International Journal for Numerical Methods in Engineering 72 (2007) 127–155.
[21] C. Miehe, E. Gürses, M. Birkle, A computational framework of configurational-force-driven brittle fracture based on incremental energy minimization, International Journal of Fracture 145 (2007) 245–259.
[22] G. Capriz, Continua with Microstructure, Springer Verlag, 1989.

[23] P.M. Mariano, Multifield theories in mechanics of solids, Advances in Applied Mechanics 38 (2001) 1–93.
[24] M. Frémond, Non-Smooth Thermomechanics, Springer Verlag, 2002.
[25] C. Miehe, Comparison of two algorithms for the computation of fourth-order isotropic tensor functions, Computers & Structures 66 (1998) 37–43.
[26] C. Miehe, M. Lambrecht, Algorithms for computation of stresses and elasticity moduli in terms of Seth–Hill's family of generalized strain tensors, Communications in Numerical Methods in Engineering 17 (2001) 337–353.
[27] T.N. Bittencourt, P.A. Wawrzynek, A.R. Ingraffea, J.L. Sousa, Quasi-automatic simulation of crack propagation for 2d lefm problems, Engineering Fracture Mechanics 55 (1996) 321–334.
[28] C. Miehe, Discontinuous and continuous damage evolution in Ogden-type large-strain elastic materials, European Journal of Mechanics A / Solids 14 (1995) 697–720.